THE JOURNAL OF PHYSICAL CHEMISTRY C

Article

pubs.acs.org/JPCC

$M_4Ag_{44}(p\text{-}MBA)_{30}$ Molecular Nanoparticles

Brian E. Conn,[†] Anil Desireddy,[†,⊥] Aydar Atnagulov,[†] Sameera Wickramasinghe,[†] Badri Bhattarai,[†] Bokwon Yoon,[‡] Robert N. Barnett,[‡] Yashar Abdollahian,[§] Yong Wah Kim,[†] Wendell P. Griffith,[†] Scott R. J. Oliver,[§] Uzi Landman,[‡] and Terry P. Bigioni*[,†,∥]

[†]Department of Chemistry and Biochemistry, University of Toledo, Toledo, Ohio 43606, United States

[‡]School of Physics, Georgia Institute of Technology, Atlanta, Georgia 30332-0430, United States

[§]Department of Chemistry and Biochemistry, University of California, Santa Cruz, Santa Cruz, California 95064, United States

[∥]School of Solar and Advanced Renewable Energy, University of Toledo, Toledo, Ohio 43606, United States

ABSTRACT: $M_4Ag_{44}(p\text{-}MBA)_{30}$ molecular nanoparticles, where M is an alkali metal, have recently been shown to have exceptional stability, which confers unique traits to this molecule. In particular, the synthesis is straightforward, produces a truly single-sized molecular product, and has a quantitative yield. Here we describe in detail the results of experimental and theoretical studies on the synthesis, structure, stability, and electronic and optical properties of $M_4Ag_{44}(p\text{-}MBA)_{30}$, including ESI-MS, NMR, optical absorption, IR, TGA, and other measurements as well as DFT and TDDFT calculations. This work deepens our understanding of this important Ag molecule, which should facilitate its use in a wide range of fundamental studies and applications.

1. INTRODUCTION

Molecular gold and silver nanoparticles[1−3] are fundamentally different than larger plasmonic metal nanoparticles. For example, if a 10 nm diameter gold or silver nanoparticle were to lose a few atoms, the properties of that nanoparticle would remain unchanged. In contrast, the loss of even a single atom would change the identity of a molecular nanoparticle, by definition. To gain a better understanding of this distinct class of nanomaterials, and in particular their stability, it is important to identify and study the exceptional examples. In the case of gold, this includes $NaAu_{25}L_{18}$,[4−6] $Au_{38}L_{24}$,[7,8] and $Au_{144}L_{60}$,[9,10] whereas for silver it includes $Ag_{32}L_{19}$[11,12] and $Na_4Ag_{44}L_{30}$,[3,13−17] where L is the ligand and Na was chosen as the counterion for the species that are known to be anionic.

Silver has been used historically as a coinage metal due to its ability to endure centuries of use. The resistance to corrosion of bulk silver can be lost in nanoparticle form, however, presumably because the larger surface area of nanoparticles can accelerate oxidation. While colloidal gold nanoparticles produced by Michael Faraday[18] are still stable today, similar sized silver nanoparticles survive for only a small fraction of that time despite benefitting from the same charge stabilization mechanism.[18,19]

The stability of molecular nanoparticles is far worse than their colloidal counterparts, however, since the loss of a single atom changes the identity of the molecule. The ability of molecular nanoparticles to convert to other sizes and structures along with metal−thiolates provides a mechanism for this chemical transformation, thereby facilitating decay for both gold and silver.[4,20] Silver is more susceptible to oxidation; therefore, molecular silver nanoparticles are in general less stable than molecular gold nanoparticles.

It was recently discovered that $M_4Ag_{44}(p\text{-}MBA)_{30}$ nanoparticles (here M is an alkali metal) are actually more stable than their molecular gold nanoparticle counterparts.[3] This surprising stability has been attributed to a closed electronic shell with a large HOMO−LUMO gap, an ultrastable 32-silver-atom excavated-dodecahedral core, coordinating solvent molecules, and protective Ag_2S_5 capping structures called "mounts", a term taken from the decorative arts. $M_4Ag_{44}(p\text{-}MBA)_{30}$ belongs to a family of $Ag_{44}L_{30}$ compounds,[3,13−17] where L is a phenyl-containing thiolate ligand.

The exceptional stability of $M_4Ag_{44}(p\text{-}MBA)_{30}$ has several important consequences. First, $M_4Ag_{44}(p\text{-}MBA)_{30}$ was found to be inert under reaction conditions; therefore the product contained only a single species, which eliminated the need for separation. This was presumably a consequence of the product being much more energetically favored than any other competing structure. Second, the selectivity of the reaction for $M_4Ag_{44}(p\text{-}MBA)_{30}$ results in quantitative yields. Third, due to the aforementioned points the reaction is easily scaled to efficiently produce very large quantities of pure $M_4Ag_{44}(p\text{-}$

Special Issue: Current Trends in Clusters and Nanoparticles Conference

Received: December 9, 2014
Revised: February 24, 2015
Published: February 26, 2015

DOI: 10.1021/jp512237b
J. Phys. Chem. C 2015, 119, 11238−11249

MBA)$_{30}$ product, as shown in Figure 1. Here, we present a detailed study of the synthesis and properties of M_4Ag_{44}(p-

Figure 1. M_4Ag_{44}(p-MBA)$_{30}$ product. M_4Ag_{44}(p-MBA)$_{30}$ nanoparticles shown in solid and in solution forms. The dice represent the four Platonic solids that can be found in the structure (photo credit: Daniel Miller).

MBA)$_{30}$ molecular nanoparticles using both experiment and theory to better understand this important silver nanoparticle. Key issues such as the role of the coordinating solvent are also addressed along with the general stability and decay of the particles.

2. EXPERIMENTAL SECTION

2.1. Chemicals. Sodium borohydride, ethanol, methanol, toluene, *N*,*N*-dimethylformamide (DMF), dimethyl sulfoxide (DMSO), pyridine, acetone, citric acid, acetic acid, sodium chloride, sodium hydroxide, and cesium hydroxide were purchased from Fisher. Silver nitrate, 4-mercaptobenzoic acid (p-MBA), and ammonium acetate were purchased from Sigma-Aldrich. Cetyltrimethylammonium bromide (CTAB) was purchased from Alfa Aesar. All reagents were used as received, without further purification. Deionized water (18.2 MΩ cm) was used.

2.2. Synthesis. Briefly, 0.75 mmol of $AgNO_3$ and 1 mmol of p-MBA were added to 33 mL of 7:4 water−ethanol solvent and stirred for about 5 min followed by ∼2 min of ultrasonication. These reagents reacted to form a cloudy light yellow precipitate, which was the Ag−thiolate precursor. The pH was then adjusted to 12 using 50% w/v aqueous CsOH. The precursor dissolved when the pH was above 9, forming a clear, light yellow solution. Next, 7.5 mmol of $NaBH_4$ reducing agent in 9 mL of water was added dropwise over a period of 30 min and was left to stir for 1 h. Once the reaction was complete, the dark red solution was centrifuged for 5 min and then separated from the insoluble byproducts by decanting. Next, the product was precipitated using DMF and separated from the supernatant by centrifugation and decanting. It is important not to dry this raw product.

The raw product was an alkali metal salt of the final product since some of the carboxylates on the p-MBA ligands had sodium or cesium counterions in place of their protons. This material was protonated in DMF using an acid (e.g., acetic acid, citric acid, ascorbic acid, sulfuric acid) to displace the alkali metal cations. To protonate, pure DMF was added to the precipitated particles, which did not initially solubilize. Glacial acetic acid was then added dropwise to the solution until the precipitate dissolved into the DMF, forming a deep red solution. Protonation was repeated 3 times, precipitating with toluene each time. Once fully protonated, the final product contained only four alkali metal cations, which served as the counterions to the 4− charge on the metal core.

The final product dissolved readily into DMF without the aid of an acid. Further, it was possible to form toluene solutions of the final product, after complete protonation, although with lower concentrations than with DMF. More concentrated toluene solutions could be made using small amounts of DMF as a cosolvent. To improve shelf life of the final product, samples were stored as damp sticky solids rather than completely dry and free-flowing powders since a coordinating solvent is needed to protect the nanoparticles.

2.3. Electrospray Ionization Mass Spectrometry (ESI-MS). A Synapt HDMS quadrupole time-of-flight ion mobility mass spectrometer (Waters Corp.) was used for the collection of all mass spectrometry data.[12] The instrument was equipped with a nanospray source with negative ionization and operated in V-mode using continuous-flow fused silica emitters that were made in house. Instrumental parameters were: capillary voltage, 2.0−4.0 kV; sampling cone, 15 V; extraction cone, 4.0 V; cone gas flow rate, 0 L/h; trap collision energy, 0.5 V; transfer collision energy, 1.0 V; source temperature, 40 °C; desolvation temperature, 120 °C. External calibration was performed in the range $100 \leq m/z \leq 4000$ using cesium iodide. Approximately 600 scans were averaged and processed using Masslynx 4.1 software (Waters Corp.). Samples were protonated using citric acid and dissolved in DMF, with a concentration of approximately 0.5 mg/mL.

2.4. Optical Absorption Spectroscopy. Solutions were prepared in neat DMF or DMSO solvents. Optical absorption spectra were recorded on a PerkinElmer Lambda 950 spectrophotometer using 5 mm path length quartz cuvettes. The molar absorptivity was measured by preparing a solution with a known mass of damp solid and then determining the silver metal fraction of that mass by thermal gravimetric analysis.

For the spectral evolution during the synthesis, a dilute reaction mixture (1/8 conc.) was made, and the entire amount of $NaBH_4$ was added in ∼30 s. As the reaction proceeded, 0.5 mL aliquots were taken, centrifuged, and placed in a 1 mm path length cuvette to record the absorption spectra.

2.5. NMR. Fully protonated M_4Ag_{44}(p-MBA)$_{30}$ nanoparticles were cleaned of residual acetic acid for use in NMR experiments. To clean the nanoparticles, they were redissolved in neat DMF, precipitated with toluene, and then washed with toluene to remove the residual DMF. The clean precipitate was dried under flowing nitrogen for approximately 6 h to remove the toluene. A DMF-d_7 solution was prepared from the dried nanoparticles with a concentration of 5 mg/mL. The ^{1}H NMR spectra were collected on a Bruker Avance III 600 MHz spectrometer.

2.6. Thermogravimetric Analysis. Thermograms were obtained by heating ∼22 mg of sample in a Pt pan under a nitrogen atmosphere, ramping the temperature at 2 °C/min from room temperature to 1000 °C. This was performed with an SDT Q600 thermogravimetric analyzer from TA Instruments. For thermograms with mass analysis (TGA-MS), samples were heated in a TA Instruments 2050 TGA, heating from 25 to 1000 °C under Ar purge at a rate of 5 °C/min. Mass spectra were acquired using a Pfeiffer Vacuum ThermoStar

DOI: 10.1021/jp512237b
J. Phys. Chem. C 2015, 119, 11238−11249

GSD 301 T3 mass spectrometer with a 70 eV ionization potential.

2.7. Infrared Spectroscopy. The silver−thiolate precursor was washed twice with water and three times with ethanol to remove unreacted material and then dried and desiccated overnight. The dry precursor was mixed with dry KBr powder in a 1:50 ratio and formed into a pellet. Infrared spectra were recorded on a PerkinElmer Spectrum Two FT-IR spectrometer.

2.8. Stability Measurements. A DMSO solution of protonated M_4Ag_{44}(p-MBA)$_{30}$ nanoparticles was prepared with a concentration of 2.0 mg/mL. A 10 mL aliquot was stored in a 15 mL sample vial on the lab benchtop. For each measurement, a 0.5 mL aliquot was pipetted out and centrifuged at 5000 rcf for 5 min to remove precipitates before recording the absorption spectra in a 1 mm path length cuvette.

For oxygen-free stability experiments, a stock solution was prepared in DMSO such that the absorbance at 490 nm was 1.5 for a 1 mm path length cuvette. To this solution, 0.5 mM NaCl and 0.25 mM ammonium acetate were added. The solution was then purged with N_2 gas. The solution was split into 12 equal parts (1.5 mL each), placed in capped vials, and purged again with N_2 gas before storage. Spectra for each time point were recorded using freshly sealed solutions, which were centrifuged at 5000 rcf for 1 min before recording the absorption spectra in a 1 mm path length cuvette.

2.9. Theoretical. The density functional theory (DFT) calculations for Bader charge analysis[21,22] were performed using the VASP-DFT package with a plane-wave basis with a kinetic energy cutoff of 400 eV, PAW pseudopotentials,[23] and the PW91 generalized gradient approximation (GGA) for the exchange-correlation potential.[24−26] For structure optimization, convergence was achieved for forces smaller than 0.001 eV/Å. The X-ray determined structure of Na_4Ag_{44}(p-MBA)$_{30}$ was taken as the starting configuration for structural relaxation. Hydrogen atoms were added to the structure, and their positions were relaxed, yielding d(C−H) = 1.09 Å.

The calculations of the absorption spectra were carried out following the time-dependent density-functional theory (TDDFT) method with the formalism described in refs 27 and 28, implemented in the real-space Octopus code.[29,30] These calculations employed the norm-conserving nonlocal soft Troullier−Martins pseudopotentials[31] (including the valence electrons for the elements in the molecule: Ag ($4d^{10}5s^1$), S ($3s^2$ $3p^4$), C ($2s^2$ $2p^2$), O ($2s^2$ $2p^4$), H ($1s^1$), Na ($3s^1$)), using the generalized gradient-corrected PBE exchange−correlation (xc) potential.[32]

The Na_4Ag_{44}(p-MBA)$_{30}$ structure was relaxed with the use of the Born−Oppenheimer density functional theory (BODFT) code,[33] employing the above soft pseudopotentials and PBE xc potential. In the subsequent absorption spectra calculations the system was placed in a sphere of radius 21 Å such that the electron vanishes outside of that sphere. The grid spacing was taken as 0.2 Å, which corresponded to a 70 Ry plane-wave kinetic energy cutoff. The calculation involved 2018 valence electrons. In the TDDFT calculations, we have used all states in the interval $E_F \pm 3.1$ eV, which was chosen to coincide with minima in the density of states. This interval included 175 occupied states and 80 unoccupied states and therefore 14 000 pairs. Convergence was tested by varying the number of states included in the spectral calculations.

3. RESULTS AND DISCUSSION

3.1. Synthesis. The strategy for synthesizing M_4Ag_{44}(p-MBA)$_{30}$ nanoparticles involves the reduction of a silver−thiolate precursor in semiaqueous solution in the presence of a coordinating solvent, which helps protect the molecules. The silver−thiolate precursor forms upon combination of silver ions and p-MBA, with p-MBA in excess, precipitating at neutral pH. Increasing the pH with CsOH solubilizes the silver−thiolate to create a more homogeneous starting material, although this is not required to produce M_4Ag_{44}(p-MBA)$_{30}$ nanoparticles. It is required, however, to raise the pH to ∼12 when using water/alcohol solvents in order to deprotonate the alcohol. Note that if the reaction is carried out in an alcoholic solution at a pH that is much lower than 12 reduction with $NaBH_4$ will be vigorous (e.g., vigorous bubbling is observed), which could result in the formation of a black precipitate rather than the red product. If the pH is higher than 12, however, the reaction will require a larger amount of $NaBH_4$. While other alkali metal hydroxides can also be used, CsOH was found to produce a higher yield. Both Na^+ and Cs^+ ions are present during the reaction; therefore, the formula of the fully protonated final product is written as M_4Ag_{44}(p-MBA)$_{30}$ to represent a mixture of alkali counterions. When the reaction is done in solutions containing only Na^+ ions, the final product is Na_4Ag_{44}(p-MBA)$_{30}$.

Normally the precursor is assumed to be a silver−thiolate polymer;[34] however, in this case the p-MBA ligands could alternatively form a dimer complex that is analogous to silver benzoate.[35] Raising the pH to 9 solubilized the precursor, which seemed to indicate that the thiol groups were deprotonated and that it was the carboxylates that bound the silver ions.[36] IR spectra of the precursor contained characteristic features of a free carboxylate, however, as shown in Figure 2. The peaks near 1300 cm^{-1} and at 1427 cm^{-1} were assigned

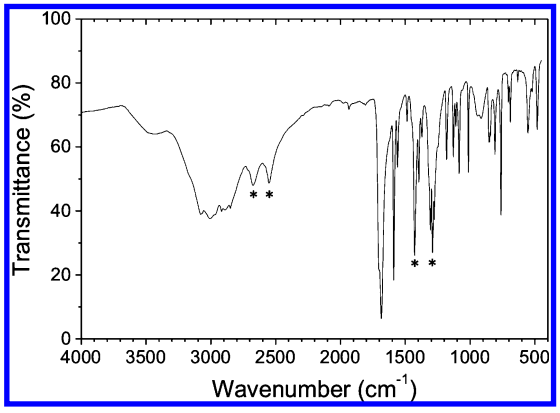

Figure 2. Silver−thiolate precursor. Infrared spectrum of the precursor contains peaks characteristic of a free carboxylate, which are indicated as *.

to C−O−H bending modes, and the two peaks between 2500 and 2700 cm^{-1} were assigned to carboxylic acid stretching modes.[37] Both cases indicate that the carboxylic acid groups were protonated and that the silver ions were bound to sulfur; therefore the precursor would be in the form of the silver−thiolate polymer.

Whether the silver−thiolate is solubilized or not, its reduction produces the same deep red solutions of M_4Ag_{44}(p-MBA)$_{30}$ nanoparticles, as shown in Figure 1. The characteristic optical absorption spectrum (see Figure 3 and Section 3.7

DOI: 10.1021/jp512237b
J. Phys. Chem. C 2015, 119, 11238−11249

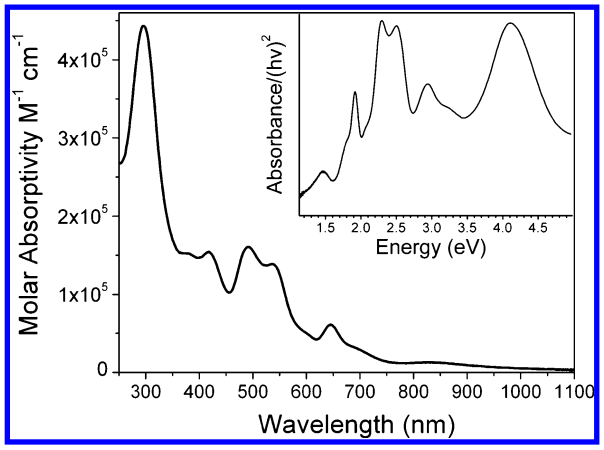

Figure 3. M_4Ag_{44}(p-MBA)$_{30}$ final product. Molar absorptivity of M_4Ag_{44}(p-MBA)$_{30}$ in DMF solution. Inset: absorbance as a function of energy.

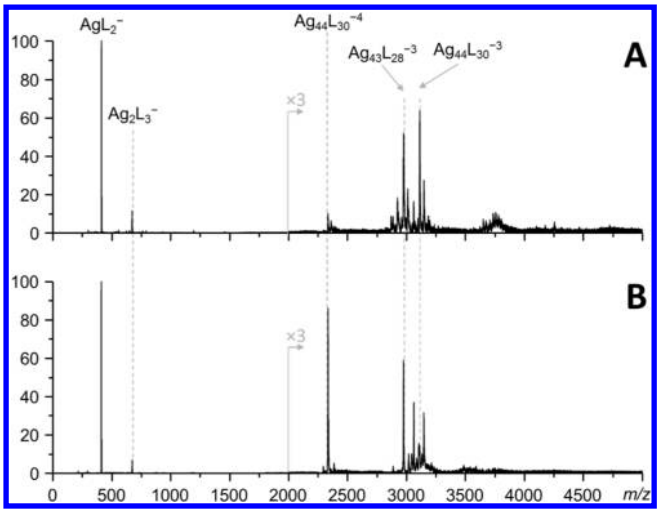

Figure 4. ESI-MS of M_4Ag_{44}(p-MBA)$_{30}$. (A) Raw product, containing excess alkali metal counterions. (B) Fully protonated final product.

below) can be used to evaluate the success of the reaction since the absorbance provides a measure of the yield and since the highly structured spectra are indicative of the purity of the product, in that it contains only a single species. The M_4Ag_{44}(p-MBA)$_{30}$ product is unique in this sense, as no processing or size sorting is required to get a precisely single-sized molecular product.

The M_4Ag_{44}(p-MBA)$_{30}$ nanoparticles were synthesized in the presence of alkali metal ions; therefore, the raw product was the conjugate base of the final product. In this case, the protons on some of the carboxylate groups on the raw product were replaced by alkali metal counterions such that the number of alkali metal atoms (identified by elemental analysis) was in excess of the four stoichiometric counterions.[3] Further, when the raw product was dissolved in semiaqueous solvents the pH was increased, indicating that it was the conjugate base of the acidic final product. The raw product readily dissolved in polar solvents but did not dissolve in nonpolar solvents.

The alkali metal counterions on the carboxylates were easily displaced by protons using acids to produce the fully protonated final product. Once protonated, the molecules dissolved readily in a variety of polar aprotic solvents such as DMF, DMSO, and pyridine. The final product could also dissolve in toluene when a small amount of coordinating solvent was added. The fully protonated nanoparticle contained four stoichiometric alkali metal cations to balance the 4− charge of the metal core. This was previously shown by elemental analysis and by high-resolution mass spectrometry of the final product, wherein all protons were precisely accounted for.[3]

Protonation was found to improve the stability of the 4− ion in the gas phase. Figure 4(A) shows the ESI mass spectrum of M_4Ag_{44}(p-MBA)$_{30}$ in DMF for the raw product. In this case, the parent peak at m/z 2335 was easily detected; however, its intensity was 5 and 6 times lower than the daughter peaks Ag_{43}(p-MBA)$_{28}^{3-}$ at m/z 2975 and Ag_{44}(p-MBA)$_{30}^{3-}$ at m/z 3115, respectively. Note that the complementary Ag_{43}(p-MBA)$_{28}^{3-}$ and AgL_2^- fragments were previously shown to result from the spontaneous fragmentation of desolvated Ag_{44}(p-MBA)$_{30}^{4-}$ ions in the gas phase.[3]

Figure 4(B) shows that the ESI-MS was significantly improved after protonation with citric acid (three times). The relative abundance of the Ag_{44}(p-MBA)$_{30}^{4-}$ parent species dramatically increased, such that it became the highest intensity peak. The increase in Ag_{44}(p-MBA)$_{30}^{4-}$ relative to the Ag_{43}(p-MBA)$_{28}^{3-}$ fragment indicated that protonation had a stabilizing effect on Ag_{44}(p-MBA)$_{30}^{4-}$. The overall reduction in fragmentation also indicated that protonation significantly improved the gas-phase stability of Ag_{44}(p-MBA)$_{30}^{4-}$ ions.

The solution-phase structure of the Ag_{44}(p-MBA)$_{30}^{4-}$ ligand shell was probed by ^{1}H NMR in DMF-d_7. The four aromatic protons of p-MBA were easily identified by their characteristic chemical shifts. The four aromatic protons of the free ligand appear as a pair of doublets, one for each chemically equivalent proton, at 7.908 and 7.513 ppm for DMF-d_7. These free ligand peaks are far upfield and have a separation that is close to 10 times larger compared with those of the bound ligands on Ag_{44}(p-MBA)$_{30}^{4-}$, as seen in Figure 5. The ^{1}H NMR of Ag_{44}(p-MBA)$_{30}^{4-}$ shows that there are two pairs of doublets with a ratio of integrated areas of 4:1 (see Figure 5), which was assigned to the four ligands at the base of each mount and the one bridging ligand at the apex of each mount (see ref 3 and Section 3.5 below). The doublets due to the four equivalent ligands appeared downfield of those of the bridging ligands, which is consistent with the more exposed bridging ligand experiencing less shielding from neighboring phenyl rings.

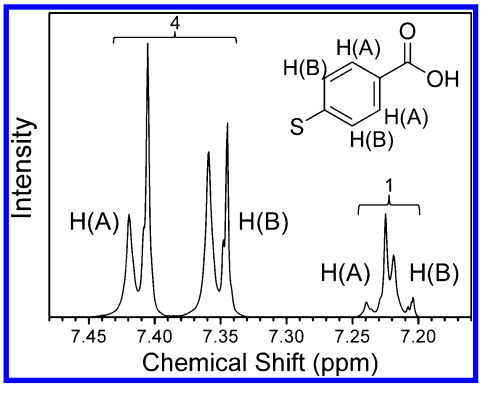

Figure 5. ^{1}H NMR of M_4Ag_{44}(p-MBA)$_{30}$ in DMF. Aromatic region of the spectrum with peaks for protons in two positions on the phenyl rings, labeled H(A) and H(B). Integrations are shown for the four ligands at the base of the mounts (peaks at left) and the bridging ligand (peaks at right). Inset shows ligand structure.

DOI: 10.1021/jp512237b
J. Phys. Chem. C 2015, 119, 11238−11249

3.2. Coordinating Solvent. The role of the coordinating solvent was studied by synthesizing the nanoparticles in semiaqueous solutions with a variety of coordinating cosolvents. Yields were quantitative for a variety of coordinating agents, including acetate, pyridine, DMSO, and DMF; therefore, it was not possible to differentiate between the effectiveness these of species. Instead, the yield of the reaction was measured for aqueous reaction mixtures that contained a minimal amount of coordinating agent, namely, 19.7 mM, which provided each M_4Ag_{44}(p-MBA)$_{30}$ nanoparticle with 48 coordinating molecules (assuming 100% yield). The yields of these reactions corresponded approximately to coordinating ability,[38] in the order acetate (94%) > DMSO (76%) ≈ DMF (76%) ≈ pyridine (75%) > pH 12 water (56%) > acetone (26%). All reactions produced the same M_4Ag_{44}(p-MBA)$_{30}$ product regardless of the coordinating solvents used with the exception of acetone, which also produced plasmonic nanoparticles. It is worth noting that using neat coordinating solvents would seem to be desirable, and semiaqueous solvents are preferred due to solubility requirements of the reagents as well as the poor activity of nonaqueous sodium borohydride.

3.3. Stability. The fact that the M_4Ag_{44}(p-MBA)$_{30}$ nanoparticle product is truly single-sized is unique among nanoparticle syntheses. Several methods exist that narrow the size distribution to essentially one nanoparticle size, but they still require either size sorting or attrition to purify the molecular product. Further, the M_4Ag_{44}(p-MBA)$_{30}$ molecular nanoparticle is immune to variations in the synthesis conditions; therefore, it is not possible to produce other sizes of Ag:p-MBA nanoparticles from the reaction. This result implies that M_4Ag_{44}(p-MBA)$_{30}$ is significantly more stable than any other size and structure that might form during the synthesis, effectively outcompeting all other species. Indeed, it was previously shown that M_4Ag_{44}(p-MBA)$_{30}$ nanoparticles are exceptionally stable, even more so than gold nanoparticles of a similar size and structure,[3] which is indicative of the remarkable selectivity of the synthesis.

To better understand the nature of the selectivity, it is useful to contrast this synthesis with the standard model of nucleation and growth of nanoparticles. In 1950, LaMer and Dinegar gave a thermodynamic description of the nucleation and growth of "monodispersed hydrosols",[39] which provided the framework for the first controlled synthesis of colloidal nanoparticles.[40] Their strategy was to separate nucleation and growth in time, such that nucleation only occurs once at the beginning of the reaction. If further nucleation is suppressed, then the reaction enters the growth stage wherein all of the nuclei grow for the same length of time and thereby accumulate the same amount of mass, resulting in monodisperse nanoparticles. This method is quite effective at producing narrow size distributions; however, the products do not have molecular precision.

The synthesis of M_4Ag_{44}(p-MBA)$_{30}$ results in a truly single-sized product with quantitative yield. On the basis of the fact that the yield is quantitative, it can be concluded that the monodispersity is not a result of attrition; that is, the size distribution was not simply narrowed by postprocessing to eliminate the least stable species. Rather, the reaction pathway leads immediately to the production of M_4Ag_{44}(p-MBA)$_{30}$ nanoparticles. This is reflected in the fact that the shape of the absorption spectrum does not evolve, but instead the molecular spectrum of the final product is immediately observed and simply grows in time, as shown in Figure 6.

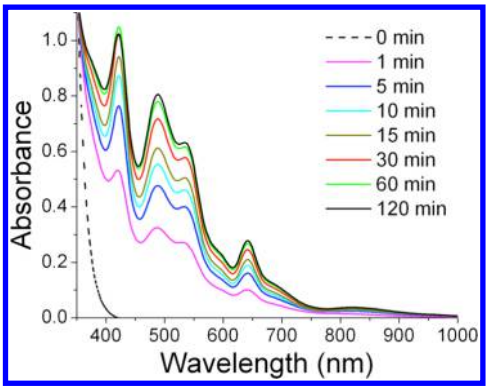

Figure 6. Spectral evolution during M_4Ag_{44}(p-MBA)$_{30}$ synthesis. Silver−thiolates at 0 min are reduced to immediately form M_4Ag_{44}(p-MBA)$_{30}$ nanoparticles, with characteristic spectra observed beginning after 1 min and persisting for the entire reaction (∼1 h). The lack of evolution of the spectral form indicates that only one species was produced.

The reason for the monodispersity of M_4Ag_{44}(p-MBA)$_{30}$ nanoparticles is fundamentally different from the conventional methodology.[39,40] Conventional size control is accomplished by restricting nucleation to only a short time at the beginning of the synthesis. In the case of M_4Ag_{44}(p-MBA)$_{30}$ nanoparticle synthesis, however, nucleation occurs over the course of the entire synthesis. Figure 6 shows that M_4Ag_{44}(p-MBA)$_{30}$ nanoparticles form at all stages of the reaction, behaving as inert spectators once formed.[3]

The fact that M_4Ag_{44}(p-MBA)$_{30}$ nanoparticles are inert under reaction conditions indicates that the potential well for this structure is very deep, such that it is not possible to convert it to a larger (or smaller) size under reaction conditions. As a consequence of this property, it is possible to accumulate M_4Ag_{44}(p-MBA)$_{30}$ nanoparticles while reagents continue to react. It is for this reason that it is possible to scale the reaction up to accumulate very large quantities of precisely monodisperse product, as shown in Figure 1. In principle, it ought to be possible to continuously add reagents to the reaction vessel and remove nanoparticle product in a continuous reaction scheme. Such a strategy is unheard of in nanoparticle synthesis.

The thermal stability of the powder was evaluated by TGA-MS (see Figure 7). Toluene solvent was primarily lost below 100 °C, followed by loss of the coordinating DMF solvent up to ∼170 °C. This is slightly higher than the boiling temperature of DMF, which might be due to weak coordination interactions with the silver atoms in the nanoparticle. It is also possible that the framework of the crystal lattice served as a kinetic barrier to DMF loss.[3,41] A small amount of toluene loss was detected up to ∼500 °C, for example, which is also consistent with being trapped in the framework of the crystal lattice.[3,41] The p-MBA ligand was lost between 300 and 400 °C, which is relatively high for a thiolated noble metal nanoparticle, indicating the superior stability of this material. The final product of thermal decomposition was silver metal.

3.4. Decay. Silver nanoparticles capped with glutathione have been shown to decay via a mechanism wherein the particles fall apart, producing a smaller particle at each step until it has entirely converted into other materials.[20] This is not the case with M_4Ag_{44}(p-MBA)$_{30}$ nanoparticles. It is not possible to convert M_4Ag_{44}(p-MBA)$_{30}$ nanoparticles to smaller sizes under the mildly oxidizing conditions of ambient storage. Ambient aging instead only reduces the concentration of the

DOI: 10.1021/jp512237b
J. Phys. Chem. C 2015, 119, 11238−11249

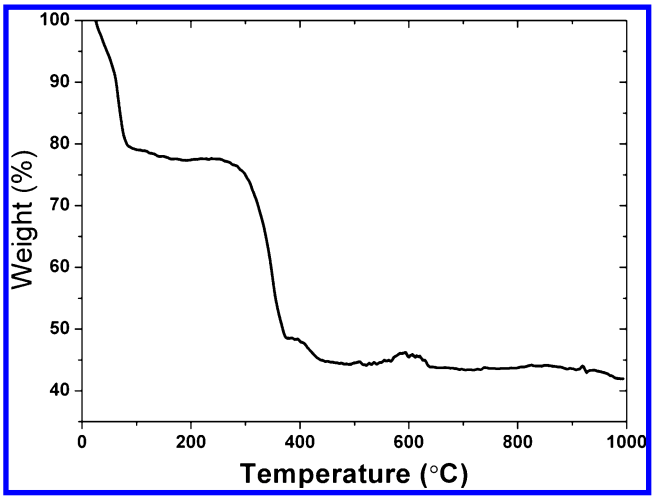

Figure 7. Thermal stability of M_4Ag_{44}(p-MBA)$_{30}$. TGA-MS of M_4Ag_{44}(p-MBA)$_{30}$ powder under Ar, showing mass losses at characteristic temperatures.

solutions and does not change their composition. This can be clearly seen in Figure 8, wherein the spectrum does not evolve

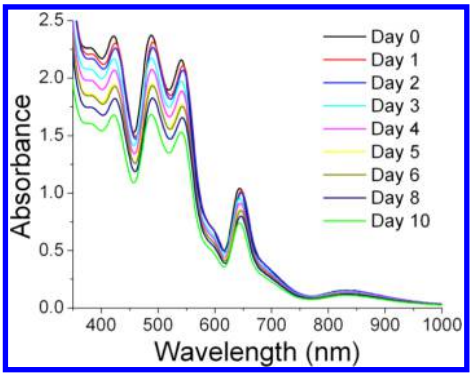

Figure 8. Ambient stability of M_4Ag_{44}(p-MBA)$_{30}$. Aged DMSO solutions of M_4Ag_{44}(p-MBA)$_{30}$ retain their characteristic spectra, indicating that no other nanoparticle species were produced. Absorbances were not rescaled.

as the solution ages, indicating that no new nanoparticle sizes were produced as a result of aging. The mechanism of decay is not yet clear; however, exclusion of oxygen improves the shelf life of M_4Ag_{44}(p-MBA)$_{30}$ nanoparticle solutions. Addition of chloride ions also improves stability, but again it is not yet clear how. Thiolates are pseudohalides;[42] therefore the chloride ions might play a ligand-like role and thereby protect the M_4Ag_{44}(p-MBA)$_{30}$ nanoparticles from oxidation.

There is a second mechanism for destabilizing M_4Ag_{44}(p-MBA)$_{30}$ that is better understood. Dissolving M_4Ag_{44}(p-MBA)$_{30}$ in neat water was found to destabilize the molecule. The absorption spectrum and electron micrograph showed that the destabilization mechanism involved the aggregation of M_4Ag_{44}(p-MBA)$_{30}$ molecules, producing larger plasmonic nanoparticles (see Figure 9). In contrast, when M_4Ag_{44}(p-MBA)$_{30}$ was dissolved in water that contained a small amount of coordinating solvent, e.g., 1% DMSO in water, the M_4Ag_{44}(p-MBA)$_{30}$ solution was stable, and no reaction was observed.

This can be understood by considering Le Chatelier's principle. For example, if M_4Ag_{44}(p-MBA)$_{30}$ precipitated from DMSO were redissolved in neat water, then the residual DMSO molecules that helped to protect the nanoparticle would leave the nanoparticle and dissolve into the solvent in order to increase the concentration of aqueous DMSO; this would remove one type of protection (NB: the chemically bound ligands are not lost when solvents are changed). With 1% DMSO in water, however, the thermodynamic driving force for deprotection and subsequent polymerization was suppressed. It is worth noting that excessive drying of the solid product can also destabilize M_4Ag_{44}(p-MBA)$_{30}$. On the basis of the solution-phase evidence, it is reasonable to assume that excessive drying could result in deprotection in the solid state, which again could lead to the polymerization of M_4Ag_{44}(p-MBA)$_{30}$.

3.5. Atomic Structure. The crystalline structure of Na_4Ag_{44}(p-MBA)$_{30}$ was determined through single-crystal X-ray diffraction measurements and theoretical analysis (see Figure 10), as reported earlier.[3] The molecule was found to have a 32 metal-atom core consisting of a hollow 12-atom icosahedral inner shell (gray spheres in Figure 10) nested within a 20-atom dodecahedral outer shell (pink spheres in

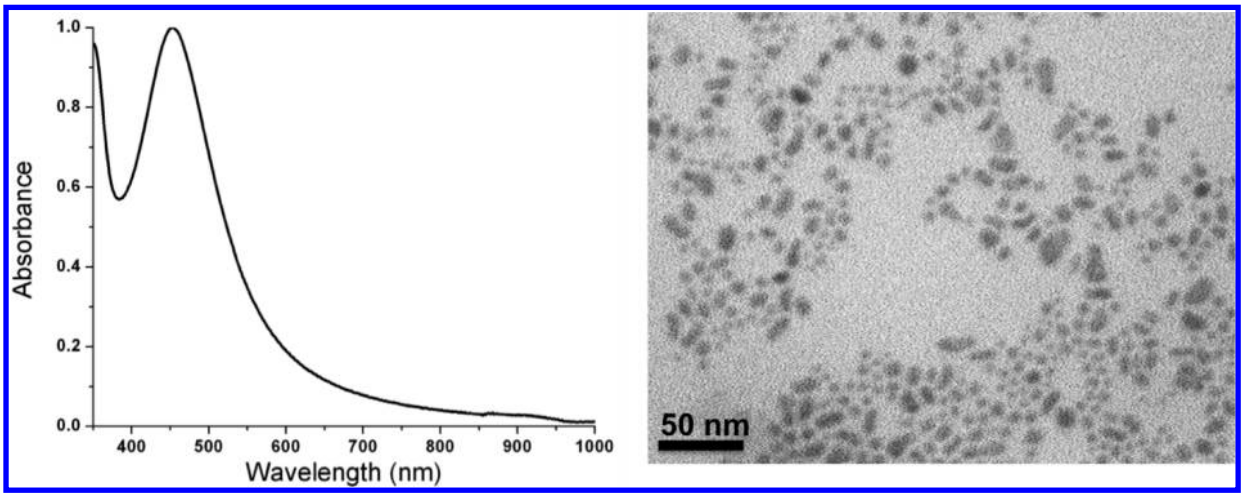

Figure 9. Polymerization of M_4Ag_{44}(p-MBA)$_{30}$. (Left) Dissolving the product in neat water leads to the formation of plasmonic Ag nanoparticles. (Right) Electron micrograph of the resultant plasmonic nanoparticles.

DOI: 10.1021/jp512237b
J. Phys. Chem. C 2015, 119, 11238−11249

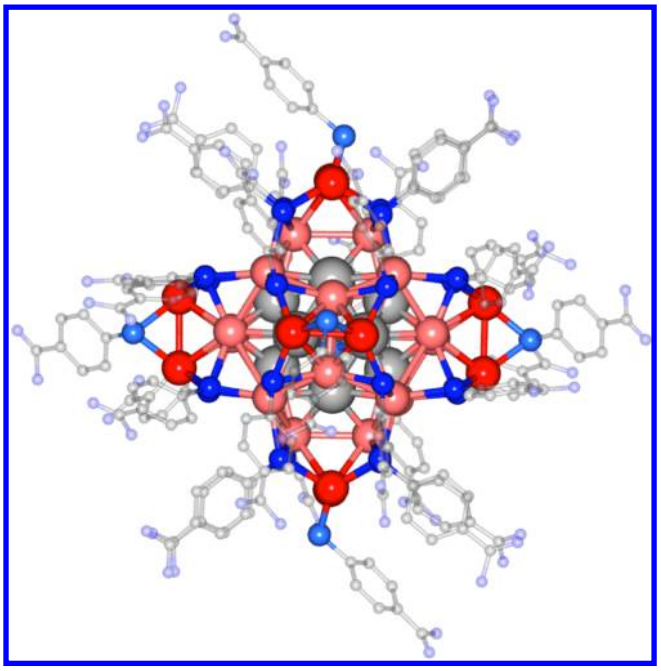

Figure 10. $Na_4Ag_{44}(p\text{-}MBA)_{30}$ atomic structure and Bader charge analysis (BCA). The structure was determined by X-ray diffraction and relaxed as $Na_4Ag_{44}(p\text{-}MBA)_{30}$. The BCA results are represented by the following color scheme: dark gray atoms are charge neutral (12 Ag atom icosahedral inner core); pink atoms (20 Ag atom dodecahedral outer core) and red (six pairs of Ag atoms in the mounts) have a net positive charge; blue atoms (S), small light gray atoms (C), and small light blue atoms (O) are negatively charged.

Figure 10), together forming a Ag_{32} excavated-dodecahedral core with icosahedral symmetry. Two distinct metal atom sites exist within the 20-atom outer shell. Eight Ag atoms within the dodecahedral outer shell define the vertices of a cube; these Ag atoms are bonded to three S atoms. The remaining 12 Ag atoms are located in pairs on the 6 faces of the 8 Ag-atom cube; each of these Ag atoms are bonded to two S atoms.

Four S atoms are located on each face of the cube such that the 24 S atoms (dark blue spheres in Figure 10) define a slightly distorted rhombicuboctahedron.[3] Each face then receives a bridging Ag_2S group to complete the inorganic part of the structure and the octahedral shape; in Figure 10, the silver atoms in the Ag_2S group are colored red, and the sulfur atom is represented by the lighter blue sphere. This arrangement of atoms creates an overall octahedral shape for the molecule, with the p-MBA ligands binding to the Ag atoms through the S atoms.

As previously noted,[3] the capping structures are unlike anything seen in Au nanoparticles[2,5,6,8,43] or in silver−thiolate materials.[42] The capping structures can be viewed as Ag_2S_5 mounts, each with four S atoms (dark blue spheres in Figure 10) acting as legs that connect them to the Ag_{32} core. The four S atoms are bridged by a pair of Ag atoms (red spheres in Figure 10) that are in turn bridged by a terminal S atom (lighter blue sphere in Figure 10), which gives the mount an overall "crested-sawhorse" shape. Altogether, six such Ag_2S_5 mounts comprise the entire layer protecting the compact, quasi-spherical Ag_{32} core.

It is important to note that the crystal structure reveals two relatively exposed Ag atoms on each of the six mounts.[3] These sites appear to demand protection, consistent with the experimental observation that $M_4Ag_{44}(p\text{-}MBA)_{30}$ requires a coordinating solvent for stability.[3] Once the protection of the coordinating solvent is lost, the molecules can polymerize to form larger plasmonic Ag nanoparticles, as described above in Section 3.4. The exposed Ag sites revealed by the crystal structure might play a role in that mechanism.

3.6. Electronic Structure. Insights into the electronic structure and optical properties of $Na_4Ag_{44}(p\text{-}MBA)_{30}$ were gained through extensive first-principles calculations. The charge distribution was obtained through Bader charge analysis (BCA)[21] of the ground-state electronic wave functions of the molecule (see Table 1 and Figure 10). The BCA provides an estimate of the local net charge in a prescribed region in the molecule by finding the difference between the number of electrons found in that region and the number of valence electrons associated with that region. Specifically, the BCA provides an estimate of the balance, $\Delta N(e^-)$, between the number of electrons, $N(e^-)$, found in a prescribed region about a selected atom or group of atoms and the number of valence electrons, $N_v(e^-)$, associated with that atom (or atoms) in that prescribed region when isolated from the molecule, such that $\Delta N(e^-) = N(e^-) - N_v(e^-)$ and the charge balance $\Delta Q(e^-) = -\Delta N(e^-)$.

The results of the BCA for the molecule, given in Table 1, show the excess ($\Delta N(e^-) > 0$), deficiency ($\Delta N(e^-) < 0$), or no change ($\Delta N(e^-) = 0$) in the number of electrons in the various prescribed regions of the molecule. The number of valence electrons considered in the pseudopotential for each of the elements was 11 for Ag, 6 for S, 4 for C, 6 for O, and 1 for H. The analysis shows that the 12 Ag atoms located in the icosahedral inner shell remain unoxidized ($\Delta N(e^-) = -0.01$), while the 20 Ag atoms in the dodecahedral outer shell of the Ag_{32} core had a deficiency of $\Delta N(e^-) = -4.92e$. This is consistent with classical electrostatics in that the charge on a metal sphere is located at its surface and not in its interior.

Table 1. Bader Charge Analysis Evaluated for the Optimal Structure of $Na_4Ag_{44}(p\text{-}MBA)_{30}$

region	$N(e^-)$	$N_v(e^-)$	$\Delta Q(e^-)$	$\Delta Q(e^-)$/unit
12 Ag in inner shell	132.01	132	−0.01	−0.001/atom
8 Ag in outer shell (cube)	85.73	88	2.266	0.283/atom
12 Ag in outer shell	129.34	132	2.658	0.222/atom
12 Ag in mounts	127.91	132	4.09	0.341/atom
inner 24 S	152.53	144	−8.53	−0.355/atom
bridging 6 S	37.71	36	−1.71	−0.285/atom
30 Ph rings	838.38	840	1.618	0.054/Ph ring
30 COOH	334.39	330	−4.388	−0.146/COOH
4 Na	0	4	4	1/atom

DOI: 10.1021/jp512237b
J. Phys. Chem. C 2015, 119, 11238−11249

This analysis also shows that the bonding between Ag and S and the resultant redistribution of charge are more complex than is commonly assumed, in part due to the complex nature of the ligand structure. The ligands are normally assumed to fully oxidize the Ag atoms to produce thiolate (i.e., RS^-) and Ag^+. In this case, the Ag atoms in the outer shell were only partially oxidized, with an average oxidation state of +0.246 rather than +1. The outer shell of the Ag_{32} core consists of two chemically distinct sites, however, with different oxidation states. The 8 Ag atoms that define the vertices of a cube are each coordinated to three thiolates and therefore have a higher oxidation state of +0.283, while the remaining 12 Ag atoms in the dodecahedral outer shell are each coordinated to two thiolates and therefore have a lower oxidation state of +0.222. This is not consistent with classical electrostatics in that the charge on a metal sphere is normally distributed evenly on its surface.

The 24 S atoms at the base of the six mounts connect directly to the Ag_{32} core and are all chemically equivalent. They had a total electron excess of 8.53*e*, and therefore their oxidation states were −0.355 rather than −1. The remaining three atoms in the mounts (Ag_2S) might be expected to be more completely oxidized/reduced since they are somewhat separated from the core. While this was true of the 12 Ag atoms in the mounts, which had an oxidation state of +0.341, this was not true of the outermost 6 S atoms atop the mounts, which had an oxidation state of −0.285.

It is interesting to note that the inorganic part of the molecule only carried a charge of −1.24*e* despite the total charge of −4*e* for the anionic part of the molecule, i.e., with no alkali metal counterions. The remainder of the negative charge was distributed across the benzoic acid portions of the ligands. The excess negative charge was located on the oxygen atoms, while the phenyl rings contained excess positive charge. Together with the four Na^+ counterions, which each had an oxidation state of +1, the total charge was zero for Na_4Ag_{44}(p-MBA)$_{30}$.

The density of the states (DOS) of the structurally optimized molecule was calculated over an extended energy range, including the Ag 4d states (−6.0 eV ≤ E ≤ −2.7 eV) as well as deeper lying states (see Figure 11). An enlarged view of the DOS in the region −4.0 eV ≤ E_F ≤ 4.0 eV is also shown in Figure 11. The outstanding feature observed in this calculation is the relatively large energy gap between the highest occupied (HOMO) and the lowest unoccupied (LUMO) molecular orbitals, Δ_{HL} = 0.78 eV, the magnitude of which is associated with chemical stability. We also denote in Figure 11 the occupied and unoccupied regions in the spectrum that contribute to the calculated optical absorption of the molecule (see below).

The projected densities of states (PDOS, see SI of ref 3 for details) was calculated via density functional theory (DFT) and was based upon the experimental configuration of the entire molecule (see Figure 12); the PDOS reflects the angular momentum (l) symmetries of the molecular orbitals, denoted as s, p, d, f, ... (corresponding to l = 0, 1, 2, 3, ...).

The wave functions of the molecule exhibit both localized and delocalized character. The bonding in the organic part of the ligands can be described in the usual way with valence bond theory and molecular orbital theory to describe the localized and delocalized orbitals. The molecular orbitals on the inorganic part of the molecule are less familiar to the chemist, however. The localized states on the inorganic part of the

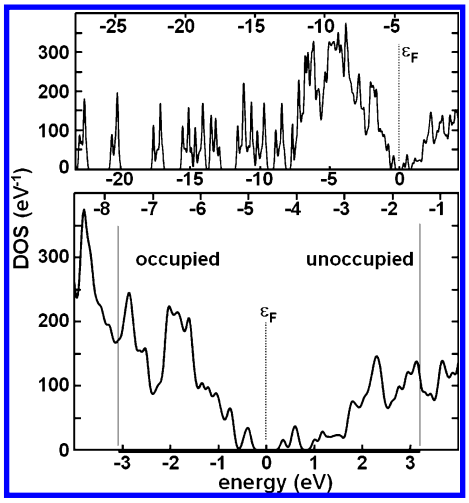

Figure 11. Calculated density of states (DOS). (Top) DOS for a structurally optimized Na_4Ag_{44}(p-MBA)$_{30}$ molecule over a broad energy range. The Fermi level, E_F, is located at the midpoint between the highest occupied KS molecular orbital (HOMO) and the lowest unoccupied KS molecular orbital LUMO. The Ag 4d states are found in the interval −6.0 eV ≤ E ≤ −2.7 eV; the other states correspond to the other constituents of the molecule. The upper energy scale is relative to the vacuum level. (Bottom) An enlarged view of the DOS near the Fermi level. The thin lines demark the two regions of width 3.1 eV labeled "occupied" and "unoccupied", which were employed in calculating optical absorption spectra.

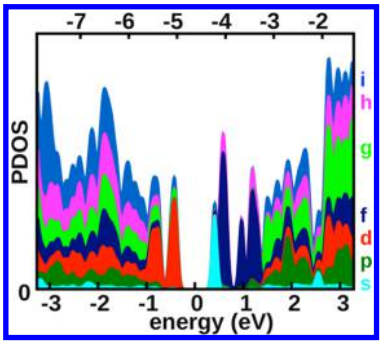

Figure 12. Nanoparticle-centered PDOS. Angular momentum projected density of states calculated for a structurally optimized Na_4Ag_{44}(p-MBA)$_{30}$ molecule. The projection into angular momentum components has been calculated with respect to the origin taken at the center of mass of the molecule. The color assignment for the angular momentum components (s, p, d, f, ...) is indicated to the right of the vertical axis. Gaussian broadening was used with a 0.05 eV halfwidth.

molecule are derived from the atomic Ag 4d electrons and the S 3p electrons and are located at the middle of the energy spectrum.[44,45]

The delocalized states on the inorganic part of the molecule are derived from the atomic Ag 5s electrons (which give rise to the conduction band in bulk silver) and can be found near the top and bottom of the electronic spectrum.[45] The appearance of the delocalized (superatom) states at the two extremes of the electronic spectrum of metal clusters was discovered in the course of an early systematic investigation[45] of gold clusters and their chemical reactivity and has been termed there as the "partial jellium model".

In our Na_4Ag_{44}(p-MBA)$_{30}$ molecule these delocalized states are spatially located primarily on the approximately spherical Ag_{32} core.[3] Since the symmetry of the core potential is similar

DOI: 10.1021/jp512237b
J. Phys. Chem. C 2015, 119, 11238−11249

to that of an atom, these molecular orbitals share the same spherical harmonics as atomic orbitals and can therefore be assigned angular momentum symmetries. These so-called superatomic orbitals follow the Aufbau rule: $1S^2 \mid 1P^6 \mid 1D^{10} \mid 2S^2 \mid 1F^{14} \mid ...$,[3,16,45−48] where the vertical lines denote shell closures; for a recent review of the cluster shell model, including the effects of deviations from spherical symmetry and applications to a broad range of finite systems, see ref 49.

For $Na_4Ag_{44}(p\text{-}MBA)_{30}$, we find delocalized 1S and 1P orbitals at −1.69 and −5.06 eV,[3] respectively. The delocalized 1D orbitals (red orbitals just below E_F in Figure 12), which are split by the (approximately) octahedral ligand field, are completely filled (i.e., it is the HOMO) making the superatomic electron configuration[3] $1S^2 \mid 1P^6 \mid 1D^{10} \mid$.

3.7. Optical Absorption. The aforementioned HOMO−LUMO energy gap Δ_{HL} = 0.78 eV does not correspond to the optical absorption threshold because the transition between the HOMO and LUMO states (1D to 2S, see Figure 12) is optically forbidden. The first calculated transition that is optically allowed corresponds to a metal-to-metal transition between the 1D HOMO to the 1F LUMO+1 states at an energy of 1.00 eV, in excellent agreement with the measured onset of optical absorption (1.08 eV, see lower inset in Figure 13).

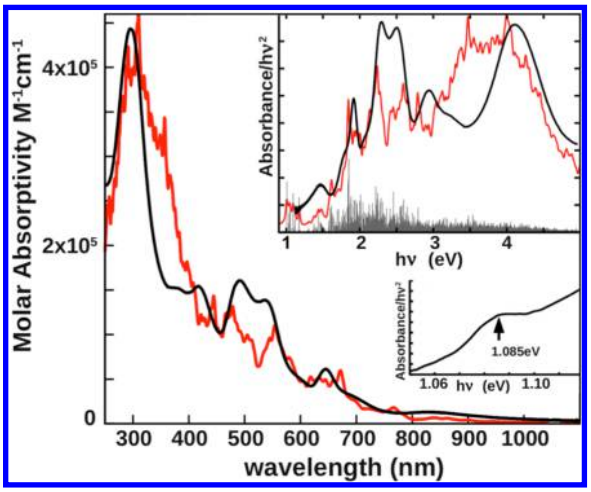

Figure 13. Optical absorption. Calculated optical absorption spectrum for a structurally optimized $Na_4Ag_{44}(p\text{-}MBA)_{30}$ molecule. (Upper inset) Calculated spectrum versus energy, obtained from the raw stick absorption spectrum (shown) by broadening with Gaussians and scaling to the experimental data. (Lower inset) Measured onset of optical absorption at 1.085 eV. Calculated spectra are shown in red, and experimental spectra are shown in black. The calculated stick spectrum (see upper inset) was broadened through the use of Lorentzians with a 0.015 eV width.

Detailed interpretation of the optical absorption spectrum requires analysis of the states and matrix elements contributing to the optical transition probabilities; see for example a method developed on the basis of time-dependent density functional perturbation theory (TD-DFPT) that allows analysis of correlations between single-particle transitions within a given energy range.[16] In the following, we give pertinent results obtained through analysis of the data obtained from our calculations. A full account about our experimental and theoretical investigations of the optical properties of the $Na_4Ag_{44}(p\text{-}MBA)_{30}$ nanoparticle will be given elsewhere.

The first significant absorption peak occurs at 1.49 eV (830 nm). This matches a calculated transition at 1.48 eV (837 nm) due to a 1D (∼−0.9 eV) to 1F (∼0.7 eV) transition with additional contributions from transitions from mixed Ag (mainly 5s) and ligand states near −1.1 eV to a 2S orbital near 0.4 eV. The next significant absorption feature occurs at 1.92 eV (645 nm) and corresponds to a calculated transition at 1.85 eV (670 nm). This originates from transitions from occupied ligand states with energies of ∼−1.4 eV to the unoccupied 1F orbital at ∼0.7 eV, with additional contributions from transitions between oxygen states at ∼−1.8 eV and the unoccupied 2S orbital.

Absorption peaks at 2.30 eV (538 nm) and 2.53 eV (490 nm) were found to correspond to calculated absorptions at 2.24 eV (553 nm) and 2.60 eV (476 nm). The lower energy (2.24 eV, 553 nm) calculated feature originates from two main sets of transitions: (a) transitions between occupied states near −1.65 and −1.70 eV having large weights on the oxygen and carbon atoms and the LUMO+1 state delocalized over the silver atoms and having a 1F superatom character and (b) transitions between occupied states having energies around −1.80 to −1.90 eV which have their largest weights mostly on the oxygen atoms and the LUMO superatom 2S state delocalized over the Ag atoms. The higher energy (2.60 eV, 476 nm) calculated feature has its origins in transitions between occupied states with energies between −1.9 and −2.1 eV having their largest weight on the carbon atoms (with some amplitude on the oxygens) and the LUMO+1 (1F) superatom orbital.

Interestingly, in the absorption spectrum calculated for the silver nanoparticle with the p-MBA ligands replaced by S-Ph (i.e., $Na_4Ag_{44}(S\text{-}Ph)_{30}$) the aforementioned 538 and 490 nm absorptions are replaced by an absorption peak centered on 506 nm (see Figure 14) deriving contributions from transitions

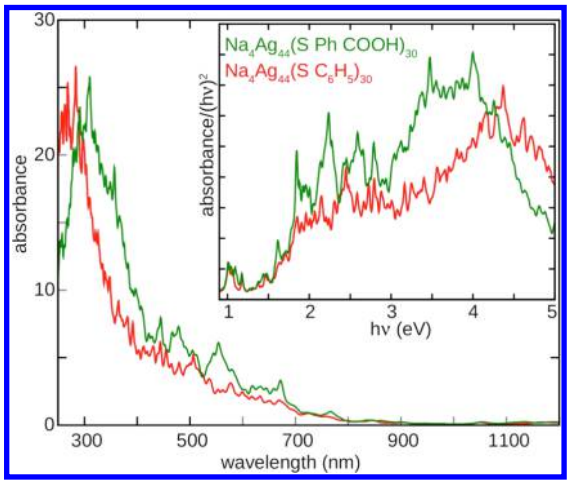

Figure 14. Ligand end-group effects on optical absorption. Spectra were calculated for energy-optimized $Na_4Ag_{44}(SR)_{30}$ structures, for both R = PhCOOH (p-MBA) shown in green and for R = Ph (C_6H_5) shown in red.

between occupied states around −1.0 eV (having amplitudes on Ag and S atoms) and the unoccupied 1F superatom state (delocalized over the Ag atoms), as well as transitions between deeper occupied states with energy near −2.2 eV (mostly on carbon atoms) and the LUMO superatom 2S state (near 0.25 eV).

DOI: 10.1021/jp512237b
J. Phys. Chem. C 2015, 119, 11238−11249

Thus far, the described optical absorption features have involved mainly transitions to the 2S and/or 1F superatomic orbitals. Higher-energy optical transitions were found to involve a wider range of unoccupied states. For example, higher energy transitions involve occupied and unoccupied states of mixed and varied nature, including ligand and superatomic states. The absorption feature observed at 2.94 eV (422nm), and calculated at 2.79 eV (444 nm) has contributions from transitions connecting occupied states near −2.25 eV (mainly on C atoms) and the superatom 2S state (at 0.35 eV) on Ag atoms, as well as from transitions between occupied states (on C atoms) at −2.25 eV and unoccupied 2F superatom states at 0.60 eV (on Ag atoms). Other contributions come from: (a) transitions between the occupied 1D superatom state (at −0.75 eV) on Ag atoms and unoccupied states (at 2.1 eV, on C atoms); (b) transitions between the superatom 1D state at −0.375 eV (on Ag) and unoccupied states (at 2.35 eV) on C and O atoms; (c) smaller and more spread contributions from transitions between occupied states (in the range of −1.6 to −1.8 eV) residing mainly on C, O and S atoms and unoccupied states in the range of 1.0 − 1.2 eV (mainly on Ag and S atom), as well as transitions between occupied states (−1.0 eV) localized mainly on Ag, S and C atoms and unoccupied states (1.75 eV) on C atoms. The prominent peak centered around 4.1 eV (or ∼300 nm) has been assigned to transitions involving states on the phenyl group, which can be seen by comparing calculated optical absorption spectra of $Na_4Ag_{44}(p\text{-}MBA)_{30}$, $Na_4Ag_{44}(SCH_3)_{30}$, and $Na_4Ag_{44}(SH)_{30}$ (see Figure 15). Finally,

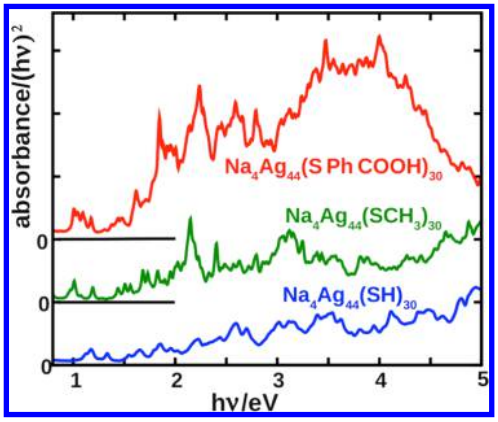

Figure 15. Ligand effects on optical absorption. Spectra were calculated for energy-optimized $Na_4Ag_{44}(SR)_{30}$ structures with different ligands, SR: red is p-MBA; green is SCH_3; blue is SH. Note that spectral features for $E \geq 3.3$ eV (red spectrum) originate mainly from the phenyl group of the p-MBA ligand.

the Ag 4d states contribute only to absorptions with energies higher than 3.5 eV. A more detailed analysis and interpretation of the optical absorption spectrum will be reported elsewhere.

We conclude our discussion of the optical absorption spectrum by noting the overall most satisfactory correspondence between the measured and calculated spectra obtained in this study, with the computed one reproducing the main features found experimentally (see Figure 13). This contrasts with the results obtained through calculations of the spectra for a 44 silver atom nanoparticle with different surface ligands, where notable discrepancies were found between the measured and theoretically calculated spectra. These discrepancies are seen in the 450−575 nm region and in the region $\lambda < 400$ nm of the spectra (see Figure 2 of ref 50 for $[Ag_{44}(SPhF)_{30}]^{4-}$, as well as Figure 3a in ref 16 where the comparison was shown for the difluoride ligand, $[Ag_{44}(SPhF_2)_{30}]^{4-}$). In particular we note that the measured double-hump spectral feature in the 450−575 nm region for $[Ag_{44}(SPhF)_{30}]^{4-}$ (which, as mentioned above, is not reproduced in the corresponding calculated spectrum, see in particular Figure 2 in ref 50) is similar to that experimentally measured and theoretically calculated by us here for the $Na_4Ag_{44}(SPhCOOH)_{30}$ nanoparticle (see Figure 13). This strongly suggests (together with the results in Figure 14) that the double-hump spectral feature is related to the electrophilic nature of the tail groups of the surface-bound ligands in the two nanoparticles (F or COOH, respectively). We remark here also that the hydrogen bonds made between the carboxylate groups of the p-MBA ligands of neighboring nanoparticles were found to confer particular stability and cohesion to the superlattice made of the $Na_4Ag_{44}(SPhCOOH)_{30}$ nanoparticles and govern its mechanical properties.[41] These observations serve to illustrate some of the subtleties and remaining challenges in calculations and interpretations of optical absorption spectra from metal nanoparticles and in particular nanoparticles with surface ligands.

4. CONCLUSIONS

We have provided details of the synthesis and processing of $M_4Ag_{44}(p\text{-}MBA)_{30}$ molecular nanoparticles, including identification of the precursor silver−thiolate compound, and have underscored the importance of coordinating solvent molecules in the synthesis and stability of this nanoparticle. The molecule was further characterized by mass spectrometry, NMR, and optical spectroscopy, including the molar absorptivity of the compound. Both temporal and thermal stability were also studied in more detail and provided mechanistic insights that might include the exposed Ag atoms in the mounts at a reaction coordinate for polymerization in the absence of coordinating molecules. Optical and electronic properties were elucidated by DFT calculations, which provided information about the different localized and delocalized molecular orbitals. Time-dependent DFT calculations were in agreement with experimental measurements and enabled assignments to be made of the features in the optical spectra, which included a wide variety of transitions between states on the core, ligand, and metal−thiolate interface. Calculations also yielded information about the distribution of charge throughout the molecule, which provided a deeper understanding of bonding at the silver−thiolate interface. This work deepens our understanding of this important silver molecule by providing insights into the atomic and electronic structure, bonding, and reactivity, which should facilitate its use in a wide range of fundamental studies and applications.

AUTHOR INFORMATION

Corresponding Author

*E-mail: terry.bigioni@utoledo.edu.

Present Address

⊥Center for Integrated Nanotechnologies, Institute for Materials Science, Los Alamos National Laboratory, Los Alamos, NM, USA 87545.

Notes

The authors declare no competing financial interest.

DOI: 10.1021/jp512237b
J. Phys. Chem. C 2015, 119, 11238−11249

■ ACKNOWLEDGMENTS

Work at the University of Toledo was supported by NSF grant CBET-0955148 as well as by the Wright Center for Photovoltaics Innovation and Commercialization and the School of Solar and Advanced Renewable Energy. The work of BY (Gatech) has been supported by the Air Force Office of Scientific Research (AFOSR) grant FA9550-14-1-0005 and the work of RNB and UL (Gatech) by the Office of Basic Energy Sciences of the US Department of Energy (DOE) under contract FG05-86ER45234. Computations were made at the GATECH Center for Computational Materials Science.

■ REFERENCES

(1) Whetten, R. L.; Khoury, J. T.; Alvarez, M. M.; Murthy, S.; Vezmar, I.; Wang, Z. L.; Stephens, P. W.; Cleveland, C. L.; Luedtke, W. D.; Landman, U. Nanocrystal Gold Molecules. *Adv. Mater.* **1996**, *8*, 428−433.

(2) Jadzinsky, P. D.; Calero, G.; Ackerson, C. J.; Bushnell, D. A.; Kornberg, R. D. Structure of a Thiol Monolayer-protected Gold Nanoparticle at 1.1 Angstrom Resolution. *Science* **2007**, *318*, 430−433.

(3) Desireddy, A.; Conn, B. E.; Guo, J.; Yoon, B.; Barnett, R. N.; Monahan, B. M.; Kirschbaum, K.; Griffith, W. P.; Whetten, R. L.; Landman, U.; Bigioni, T. P. Ultrastable Silver Nanoparticles. *Nature* **2013**, *501*, 399−402.

(4) Shichibu, Y.; Negishi, Y.; Tsunoyama, H.; Kanehara, M.; Teranishi, T.; Tsukuda, T. Extremely High Stability of Glutathione-Protected Au_{25} Clusters Against Core Etching. *Small* **2007**, *3*, 835−839.

(5) Zhu, M.; Aikens, C. M.; Hollander, F. J.; Schatz, G. C.; Jin, R. Correlating the Crystal Structure of A Thiol-Protected Au_{25} Cluster and Optical Properties. *J. Am. Chem. Soc.* **2008**, *130*, 5883−5885.

(6) Heaven, M. W.; Dass, A.; White, P. S.; Holt, K. M.; Murray, R. W. Crystal Structure of the Gold Nanoparticle $[N(C_8H_{17})_4][Au_{25}(SCH_2CH_2Ph)_{18}]$. *J. Am. Chem. Soc.* **2008**, *130*, 3754−3755.

(7) Qian, H.; Zhu, Y.; Jin, R. Size-Focusing Synthesis, Optical and Electrochemical Properties of Monodisperse $Au_{38}(SC_2H_4Ph)_{24}$ Nanoclusters. *ACS Nano* **2009**, *3*, 3795−3803.

(8) Qian, H.; Eckenhoff, W. T.; Zhu, Y.; Pintauer, T.; Jin, R. Total Structure Determination of Thiolate-Protected Au_{38} Nanoparticles. *J. Am. Chem. Soc.* **2010**, *132*, 8280−8281.

(9) Schaaff, T. G.; Shafigullin, M. N.; Khoury, J. T.; Vezmar, I.; Whetten, R. L. Properties of a Ubiquitous 29 kDa Au: SR Cluster Compound. *J. Phys. Chem. B* **2001**, *105*, 8785−8796.

(10) Qian, H.; Jin, R. Controlling Nanoparticles with Atomic Precision: the Case of $Au_{144}(SCH_2CH_2Ph)_{60}$. *Nano Lett.* **2009**, *9*, 4083−4087.

(11) Kumar, S.; Bolan, M. D.; Bigioni, T. P. Glutathione-Stabilized Magic-Number Silver Cluster Compounds. *J. Am. Chem. Soc.* **2010**, *132*, 13141−13143.

(12) Guo, J.; Kumar, S.; Bolan, M.; Desireddy, A.; Bigioni, T. P.; Griffith, W. P. Mass Spectrometric Identification of Large Silver Cluster Compounds: the Case of $Ag_{32}(SG)_{19}$. *Anal. Chem.* **2012**, *84*, 5304−5308.

(13) Bakr, O. M.; Amendola, V.; Aikens, C. M.; Wenseleers, W.; Li, R.; Dal Negro, L.; Schatz, G. C.; Stellacci, F. Silver Nanoparticles with Broad Multiband Linear Optical Absorption. *Angew. Chem., Int. Ed.* **2009**, *48*, 5921−5926.

(14) Harkness, K. M.; Tang, Y.; Dass, A.; Pan, J.; Kothalawala, N.; Reddy, V. J.; Cliffel, D. E.; Demeler, B.; Stellacci, F.; Bakr, O. M.; McLean, J. A. $Ag_{44}(SR)_{30}^{4-}$: a Silver−thiolate Superatom Complex. *Nanoscale* **2012**, *4*, 4269−4274.

(15) AbdulHalim, L. G.; Ashraf, S.; Katsiev, K.; Kirmani, A. R.; Kothalawala, N.; Anjum, D. H.; Abbas, S.; Amassian, A.; Stellacci, F.; Dass, A.; Hussain, I.; Bakr, O. M. A Scalable Synthesis of Highly-stable and Water Dispersible $Ag_{44}(SR)_{30}$ Nanoclusters. *J. Mater. Chem. A* **2013**, *1*, 10148−10154.

(16) Yang, H.; Wang, Y.; Huang, H.; Gell, L.; Lehtovaara, L.; Malola, S.; Häkkinen, H.; Zheng, N. All-thiol-stabilized Ag_{44} and $Au_{12}Ag_{32}$ Nanoparticles with Single-crystal Structures. *Nat. Commun.* **2013**, *4*, 2422.

(17) Chakraborty, I.; Kurashige, W.; Kanehira, K.; Gell, L.; Häkkinen, H.; Negishi, Y.; Pradeep, T. $Ag_{44}(SeR)_{30}$: A Hollow Cage Silver Cluster with Selenolate Protection. *J. Phys. Chem. Lett.* **2014**, *4*, 3351−3355.

(18) Faraday, M. The Bakerian Lecture: Experimental Relations of Gold (and Other Metals) to Light. *Philos. Trans.* **1857**, *147*, 145−181.

(19) Israelachvili, J. *Intermolecular and Surface Forces*; Academic Press: New York, 1992.

(20) Desireddy, A.; Kumar, S.; Guo, J.; Bolan, M. D.; Griffith, W. P.; Bigioni, T. P. Temporal Stability of Magic-number Metal Clusters: Beyond the Shell Closing Model. *Nanoscale* **2013**, *5*, 2036−2044.

(21) Bader, R. F. W.: *Atoms in Molecules - A quantum theory*; Oxford University Press: New York, 1990.

(22) Tang, W.; Sanville, E.; Henkelman, G. A Grid-based Bader Analysis Algorithm Without Lattice Bias. *J. Phys.: Condens. Matter* **2009**, *21*, 084204.

(23) Kresse, G.; Joubert, D. From Ultrasoft Pseudopotentials to the Projector Augmented-wave Method. *Phys. Rev. B* **1999**, *59*, 1758−1775.

(24) Perdew, J. P.: Unified Theory of Exchange and Correlation Beyond the Local Density Approximation,. In *Electronic Structure of Solids '91*; Ziesche, P., Eschrig, H., Eds.; Akademie Verlag: Berlin, 1991; pp 11−20.

(25) Perdew, J. P.; Chevary, J. A.; Vosko, S. H.; Jackson, K. A.; Pederson, M. R.; Singhm, D. J.; Fiolhais, C. Atoms, Molecules, Solids, and Surfaces: Applications of the Generalized Gradient Approximation for Exchange and Correlation. *Phys. Rev. B* **1992**, *46*, 6671−6687.

(26) Perdew, J. P.; Chevary, J. A.; Vosko, S. H.; Jackson, K. A.; Pederson, M. R.; Singh, D. J.; Fiolhais, C. Erratum: Atoms, Molecules, Solids, and Surfaces: Applications of the Generalized Gradient Approximation for Exchange and Correlation. *Phys. Rev. B* **1993**, *48*, 4978−4978.

(27) Casida, M. E.: Time-dependent Density-functional Response Theory for Molecules. In *Recent Advances in Density Functional Methods, Part I*; Chong, D. P., Ed.; World Scientific: Singapore, 1995.

(28) Casida, M. E.: Time-Dependent Density Functional Response Theory of Molecular Systems: Theory, Computational Methods, and Functionals. In *Recent Developments and Applications of Modern Density Functional Theory*; Seminario, J. M., Ed.; Elsevier: Amsterdam, 1996.

(29) Marques, M. A. L.; Castro, A.; Bertsch, G. F.; Rubio, A. Octopus: a First-principles Tool for Excited Electron-ion Dynamics. *Comput. Phys. Commun.* **2003**, *151*, 60−78.

(30) Andrade, X.; Alberdi-Rodriguez, J.; Strubbe, D. A.; Oliveira, M. J. T.; Nogueira, F.; Castro, A.; Muguerza, J.; Arruabarrena, A.; Louie, S. G.; Aspuru-Guzik, A.; Rubio, A.; Marques, M. A. L. Time-dependent Density-functional Theory in Massively Parallel Computer Architectures: the Octopus Project. *J. Phys.: Condens. Matter* **2012**, *24*, 233202.

(31) Troullier, N.; Martins, J. L. Efficient Pseudopotentials for Plane-wave Calculations. *Phys. Rev. B* **1991**, *43*, 1993−2006.

(32) Perdew, J. P.; Burke, K.; Ernzerhof, M. Generalized Gradient Approximation Made Simple. *Phys. Rev. Lett.* **1996**, *77*, 3865−3868.

(33) Barnett, R. N.; Landman, U. Born-Oppenheimer Molecular Dynamics Simulations of Finite Systems: Structure and Dynamics of $(H_2O)_2$. *Phys. Rev. B* **1993**, *48*, 2081−2097.

(34) Dance, I. G.; Fisher, K. J.; Herath Banda, R. M.; Scudder, M. L. Layered Structure of Crystalline Compounds AgSR. *Inorg. Chem.* **1991**, *30*, 183−187.

(35) Usubaliev, B. T.; Movsumov, É. M.; Amiraslanov, I. R.; Akhmedov, A. I.; Musaev, A. A.; Mamedov, K. S. Crystal Structures of Silver(I) Benzoate and p-Hydroxybenzoate. *J. Struct. Chem.* **1981**, *22*, 73−77.

(36) Irving, R. J.; Nelander, L.; Wadsö, I. Thermodynamics of the Ionization of Some Thiols in Aqueous Solution. *Acta Chem. Scand.* **1964**, *18*, 769−787.

DOI: 10.1021/jp512237b
J. Phys. Chem. C 2015, 119, 11238−11249

(37) Johnson, S. L.; Rumon, K. A. Infrared Spectra of Solid 1:1 Pyridine-Benzoic Acid Complexes; the Nature of the Hydrogen Bond as a Function of the Acid-Base Levels in the Complex. *J. Phys. Chem.* **1965**, *69*, 74−86.
(38) Diaz-Torres, R.; Alvarez, S. Coordinating Ability of Anions and Solvents Towards Transition Metals and Lanthanides. *Dalton Trans.* **2011**, *40*, 10742−10750.
(39) LaMer, V. K.; Dinegar, R. H. Theory, Production and Mechanism of Formation of Monodispersed Hydrosols. *J. Am. Chem. Soc.* **1950**, *72*, 4847−4854.
(40) Murray, C. B.; Norris, D. J.; Bawendi, M. G. Synthesis and Characterization of Nearly Monodisperse CdE (E = S, Se, Te) Semiconductor Nanocrystallites. *J. Am. Chem. Soc.* **1993**, *115*, 8706−8715.
(41) Yoon, B.; Luedtke, W. D.; Barnett, R. N.; Gao, J.; Desireddy, A.; Conn, B. E.; Bigioni, T. P.; Landman, U. Hydrogen-bonded Structure and Mechanical Chiral Response of a Silver Nanoparticle Superlattice. *Nat. Mater.* **2014**, *13*, 807−811.
(42) Dance, I. G. The Structural Chemistry of Metal Thiolate Complexes. *Polyhedron* **1986**, *5*, 1037−1104.
(43) Zeng, C.; Qian, H.; Li, T.; Li, G.; Rosi, N. L.; Yoon, B.; Barnett, R. N.; Whetten, R. L.; Landman, U.; Jin, R. Total Structure and Electronic Properties of the Gold Nanocrystal $Au_{36}(SR)_{24}$. *Angew. Chem., Int. Ed.* **2012**, *51*, 13114−13118.
(44) Papaconstantopoulos, D. A.: *Handbook of the Band Structure of Elemental Solids*; Plenum Press: New York, 1986.
(45) Yoon, B.; Koskinen, P.; Huber, B.; Kostko, O.; von Issendorff, B.; Häkkinen, H.; Moseler, M.; Landman, U. Size-Dependent Structural Evolution and Chemical Reactivity of Gold Clusters. *ChemPhysChem* **2007**, *8*, 157−161.
(46) Knight, W. D.; Clemenger, K.; de Heer, W. A.; Saunders, W. A.; Chou, M. Y.; Cohen, M. L. Electronic Shell Structure and Abundances of Sodium Clusters. *Phys. Rev. Lett.* **1984**, *52*, 2141−2143.
(47) de Heer, W. A. The Physics of Simple Metal Clusters: Experimental Aspects and Simple Models. *Rev. Mod. Phys.* **1993**, *65*, 611−676.
(48) Chakraborty, I.; Govindarajan, A.; Erusappan, J.; Ghosh, A.; Pradeep, T.; Yoon, B.; Whetten, R. L.; Landman, U. The Superstable 25 kDa Monolayer Protected Silver Nanoparticle: Measurements and Interpretation as an Icosahedral $Ag_{152}(SCH_2CH_2Ph)_{60}$ Cluster. *Nano Lett.* **2012**, *12*, 5861−5866.
(49) Yannouleas, C.; Landman, U. *Shell-Correction and Orbital-Free Density-Functional Methods for Finite Systems*; World Scientific: Singapore, 2013; pp 203−250.
(50) Gell, L.; Häkkinen, H. Theoretical Analysis of the $M_{12}Ag_{32}(SR)_{40}^{4-}$ and $X@M_{12}Ag_{32}(SR)_{30}^{4-}$ Nanoclusters (M = Au, Ag; X = H, Mn). *J. Phys. Chem. C* **2015**, DOI: 10.1021/jp510926q.

DOI: 10.1021/jp512237b
J. Phys. Chem. C 2015, 119, 11238−11249